Acta Crystallographica Section B
Structural Science
ISSN 0108-7681

Observation of 4*f* electron transfer from Ce to B_6 in the Kondo crystal CeB_6 and its mechanism by multi-temperature X-ray diffraction

Kiyoaki Tanaka[a,b]* and Yoshichika Ōnuki[a,b]

[a]Department for Materials Science and Engineering, Nagoya Institute of Technology, Gokiso-cho, Showa-ku, Nagoya 466, Japan, and [b]Physics Department, Osaka University, Machikaneyama-cho, Toyonaka, Japan

Correspondence e-mail: kiyo@tana.mse.nitech.ac.jp

Received 16 May 2001
Accepted 18 December 2001

Electron density distributions (EDD) in CeB_6 were measured by X-ray diffraction at 100, 165, 230 and 298 K. Analysis with a weak-field model, in which the spin-orbit interaction dominates the energy splitting of the 4*f* levels, revealed that more 4*f* electrons were donated from Ce to B_6 at the lower temperature. Donated electrons localize around the B—B bonds connecting B_6 octahedra. The localized electrons and an expansion of the outermost 5*p* orbitals change the effective atomic potentials and enhance the anharmonic vibration (AHV) of constituent atoms at lower temperature. Enhanced AHV increases the entropy and makes the electron donation inevitable. Changes in crystal structure, EDD, electron configuration and AHV are found to be closely correlated with one another and the mechanism of the electron transfer in the Kondo crystal CeB_6 in the studied temperature range was elucidated. This is, to the authors' knowledge, the first multi-temperature measurement of EDD that elucidates a mechanism of change from the temperature dependence of the EDD. Parameters change consistently at all the temperatures except 298 K, at which the excited states Γ_7 of the Ce 4*f* states have significant electron population. The thermal excitation to Γ_7 levels expands the B_6 octahedra, since Γ_7 has main lobes along $\langle 111 \rangle$ or from Ce to the centre of B_6 octahedra. The energy gap between the ground state Γ_8 and Γ_7 was calculated to be 470 K from the ratio of electron populations of both states. The present experiment opens the door to accurate X-ray EDD analyses of rare earth complexes.

1. Introduction

The EDD in rare earth compounds has not often been studied because they have too many electrons and are too complex to treat with theories and experiments. However, rare earth compounds have many interesting properties that are waiting to be investigated. Research on the EDD in rare earth compounds is still one of the frontier fields in X-ray diffraction. The EDD of rare earth complexes has been measured for CeB_6 (Sato, 1985; Tanaka *et al.*, 1997; Streltsov *et al.*, 1999) among others (Chatterjee *et al.*, 1988; Makarova *et al.*, 1995; du Boulay *et al.*, 1995; Maslen *et al.*, 1996*a*,*b*; Streltsov & Ishizawa, 1999). The first analysis of 4*f* EDD based on a quantum-mechanical model was carried out for CeB_6 at 165 K, employing a strong-field model (Tanaka *et al.*, 1997; hereinafter referred to as TKŌ), and significant peaks around Ce were shown to be due to 4*f* electrons. In a strong-field model, the crystal field is dominant in determining the splitting of 4*f* levels.

© 2002 International Union of Crystallography
Printed in Great Britain – all rights reserved

36 CeB_6 has one of the most closest-packed crystal structures. Ce and B atoms are located at the body centre and on the edges, respectively, of a cubic unit cell, with the centres of B_6 regular octahedra at the corners, as illustrated in Fig. 1. Ce is located in an O_h crystal field. CeB_6 is a typical dense Kondo material. Its electrical resistivity exhibits a –log T dependence and below the Kondo temperature, T_K = 2 K, the resistivity increases to the residual resistance. The magnetic moment decreases with temperature and vanishes below T_K. Electrons delocalize below T_K, creating a heavy mass as a result of an admixture of the delocalized electrons with the *spd* conduction electrons (Ōnuki, Komatsubara *et al.*, 1989). The Kondo effect starts above room temperature (Ōnuki *et al.*, 1984). Therefore, a change in EDD with temperature is most interesting, even in the range of temperature of our experiments: 100, 165, 230 and 298 K. The first aim of the present study is to observe and analyse the EDD in the changing system with a proper quantum-mechanical model and to elucidate the mechanism of the change from the temperature dependence of the electronic states, the anharmonic vibrations and the crystal structure. The present article shows that, beyond our expectation, detailed information on the electron transfer and the accompanied movement of atoms can be obtained consistently by multi-temperature X-ray diffraction.

The measurement of changes in the EDD caused by external perturbations such as irradiated light has been attempted by many researchers, but no one has ever succeeded, largely because electron translations to excited states are always accompanied by a change in the molecular structure. Illuminated light excites electrons and then molecular structure begins to change gradually to fit to the new electronic state. Therefore, X-ray intensity measurement does not permit one to observe a clear and meaningful EDD of the excited states, only the averaged and thus obscured image of them being obtainable. However, atomic motions in CeB_6, with one of the most closest-packed crystals, are restricted and the change in molecular structure is very small. Thus, the EDD of the excited states of CeB_6 is expected to be measureable if the population of the excited electrons is large. Ce Γ_8 was experimentally confirmed to be the ground state. The energy gap between the ground state Γ_8 and the first excited state Γ_7 was estimated to be 530 K by inelastic magnetic neutron scattering (Zirngiebl *et al.*, 1984) and by a measurement of the magnetization (Sato *et al.*, 1984). Since the energy gap is small, thermal excitation of electrons to the Γ_7 state is expected to occur at 298 K. The second aim of the present study is to obtain experimental evidence of the existence of excited electrons.

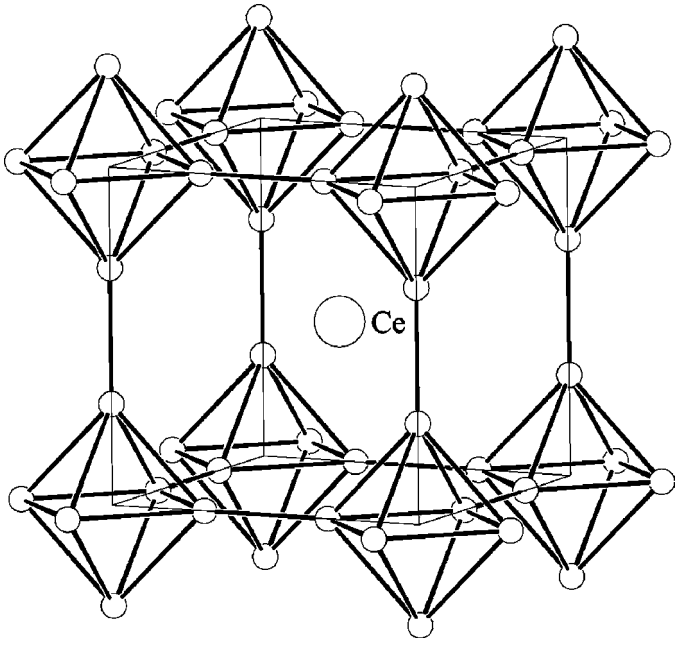

Figure 1
Crystal structure of CeB_6.

2. Experimental

Crystal and experimental data are summarized in Table 1. The same sample as reported by TKŌ was used. Measurements of the 4*f* EDD have been considered to be among the most difficult to make by X-ray diffraction, for the reasons described by TKŌ. Thus, a spherical crystal with a radius of 36 μm was used. In order to obtain reliable thermal parameters, the time spent measuring higher-order weak reflections was more than ten times that spent measuring lower-order strong reflections. The times for measurement of the background and a peak are proportional to the square-roots of their counting rates (Shoemaker, 1968), which also gave more time to higher-order reflections. Since the diffracting power per unit volume of CeB_6 is one or two orders larger than that of small organic molecules, perturbation arising from multiple diffraction easily exceeds 1% of each structure factor. The variation in the observed structure factor of 211 with the rotation angle, ψ, of the crystal around the scattering vector is represented in Fig. 2. Multiple diffraction was avoided by ψ rotation using the program *IUANGLE* (Tanaka *et al.*, 1994). Since the temperature of the sample varies with the ω and χ angles of a four-circle diffractometer (MAC Science) in low-temperature measurements with a cold nitrogen-gas flow, intensities were measured at angles where the temperature of the sample could be kept within ±1 K, as reported by TKŌ. Approximately 90% of the reflections were measured at

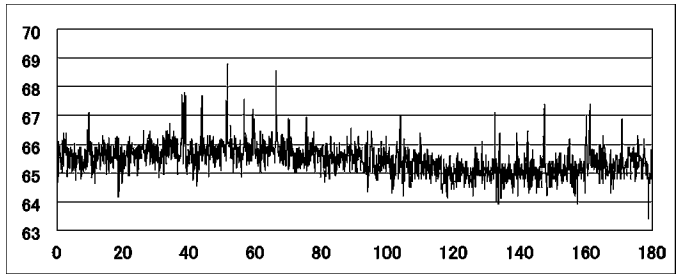

Figure 2
Observed structure factors F_o(211) measured at ψ = 0–180° at intervals of 1°.

Table 1
Crystal data and data collection details.

	100 K	165 K	230 K	298 K
Crystal data				
Chemical formula	CeB_6	CeB_6	CeB_6	CeB_6
Chemical formula weight	204.98	204.98	204.98	204.98
Cell setting, space group	Cubic, $Pm\bar{3}m$	Cubic, $Pm\bar{3}m$	Cubic, $Pm\bar{3}m$	Cubic, $Pm\bar{3}m$
a (Å)	4.1367 (1)	4.1381 (1)	4.1391 (1)	4.1407 (1)
V (Å^3)	70.788 (3)	70.862 (2)	70.914 (4)	70.996 (2)
Z	1	1	1	1
D_x (Mg m^{-3})	4.8084	4.8033	4.7999	4.7943
Radiation type	Mo $K\alpha$	Mo $K\alpha$	Mo $K\alpha$	Mo $K\alpha$
No. of reflections for cell parameters	50	50	50	50
θ range (°)	36.45–39.05	36.43–39.04	36.45–39.05	37.71–39.01
μ (mm^{-1})	16.013	15.996	15.984	15.966
Temperature (K)	100 (1)	165 (1)	230 (1)	298
Crystal form, colour	Sphere, metallic dark purple	Sphere, metallic dark purple	Sphere, metallic dark purple	Sphere, metallic dark purple
Crystal radius (mm)	0.036	0.036	0.036	0.036
Data collection				
Diffractometer	Four-circle	Four-circle	Four-circle	Four-circle
Data collection method	Integrated intensities data from $\omega/2\theta$ scans	Integrated intensities data from $\omega/2\theta$ scans	Integrated intensities data from $\omega/2\theta$ scans	Integrated intensities data from $\omega/2\theta$ scans
Absorption correction	Sphere	Sphere	Sphere	Sphere
T_{min}	0.43266	0.43304	0.43331	0.43371
T_{max}	0.48113	0.48141	0.48162	0.48193
No. of measured, independent, observed and measured at $\psi \neq 0$ reflections	1089, 167, 1063, 980	857, 187, 815, 532	841, 168, 788, 792	1079, 192, 983, 848
Criterion for observed reflections	$F > 3.0\sigma(F)$	$F > 3.0\sigma(F)$	$F > 3.0\sigma(F)$	$F > 3.0\sigma(F)$
R_{int}	0.0207	0.02356	0.00698	0.045
θ_{max} (°)	74.64	74.57	74.52	74.46
Range of h, k, l	$-10 \rightarrow h \rightarrow 11$ $-9 \rightarrow k \rightarrow 11$ $-9 \rightarrow l \rightarrow 10$	$-10 \rightarrow h \rightarrow 11$ $-10 \rightarrow k \rightarrow 11$ $-9 \rightarrow l \rightarrow 8$	$-10 \rightarrow h \rightarrow 11$ $-11 \rightarrow k \rightarrow 11$ $-4 \rightarrow l \rightarrow 10$	$-10 \rightarrow h \rightarrow 11$ $-10 \rightarrow k \rightarrow 11$ $-7 \rightarrow l \rightarrow 10$
No. and frequency of standard reflections	3 every 50 reflections	3 every 50 reflections	3 every 50 reflections	3 every 50 reflections
Intensity decay, within each reflection class (%)	0	1	0	1
Refinement				
Refinement on	F	F	F	F
No. of reflections and parameters used in refinement	1063, 24 (2 scales)	815, 23	788, 23	983, 25 (3 scales)
Weighting scheme	Unit	Unit	Unit	unit
$(\Delta/\sigma)_{max}$	0.018	0.021	0.030	0.010
$\Delta\rho_{max}$, $\Delta\rho_{min}$ (e Å^{-3})	0.38, −0.4	0.36, −0.53	0.5, −0.49	0.51, −0.41
Extinction method	B—C type 1 Gaussian anisotropic	B—C type 1 Gaussian anisotropic	B—C type 1 Gaussian anisotropic	B—C type 1 Gaussian anisotropic

positions that differed from the conventional bisecting ones. The orientation matrix and lattice parameters were determined using {155}, {336}, 444 and $\bar{4}\bar{4}\bar{4}$ with $2\theta > 70°$, where the $K\alpha$ doublet was clearly separated. The entire diffractometer was installed in an airtight box to avoid ice formation on the crystal.

3. Theoretical

X-ray diffraction data were analysed with the method called X-ray atomic orbital (AO) analysis (Tanaka, 1988, 1993). This method is based on AOs in a crystal field and is useful for quantitative analysis of localized electrons, such as d and f electrons in ionic crystals. It is also a good tool to test quantum-mechanical models. For orbitals in a high-symmetry crystal field, AOs are usually known. For low-symmetry fields, AOs are determined with a least-squares method incorporating ortho-normal relationships between orbital functions (Tanaka, 1988). In X-ray AO analysis, the ith 4f orbital $\psi_i(\kappa_i\mathbf{r})$ is defined as

$$\psi_i(\kappa_i\mathbf{r}) = \sum_k c_{ik}\varphi_k(\kappa_i\mathbf{r}), \quad (1)$$

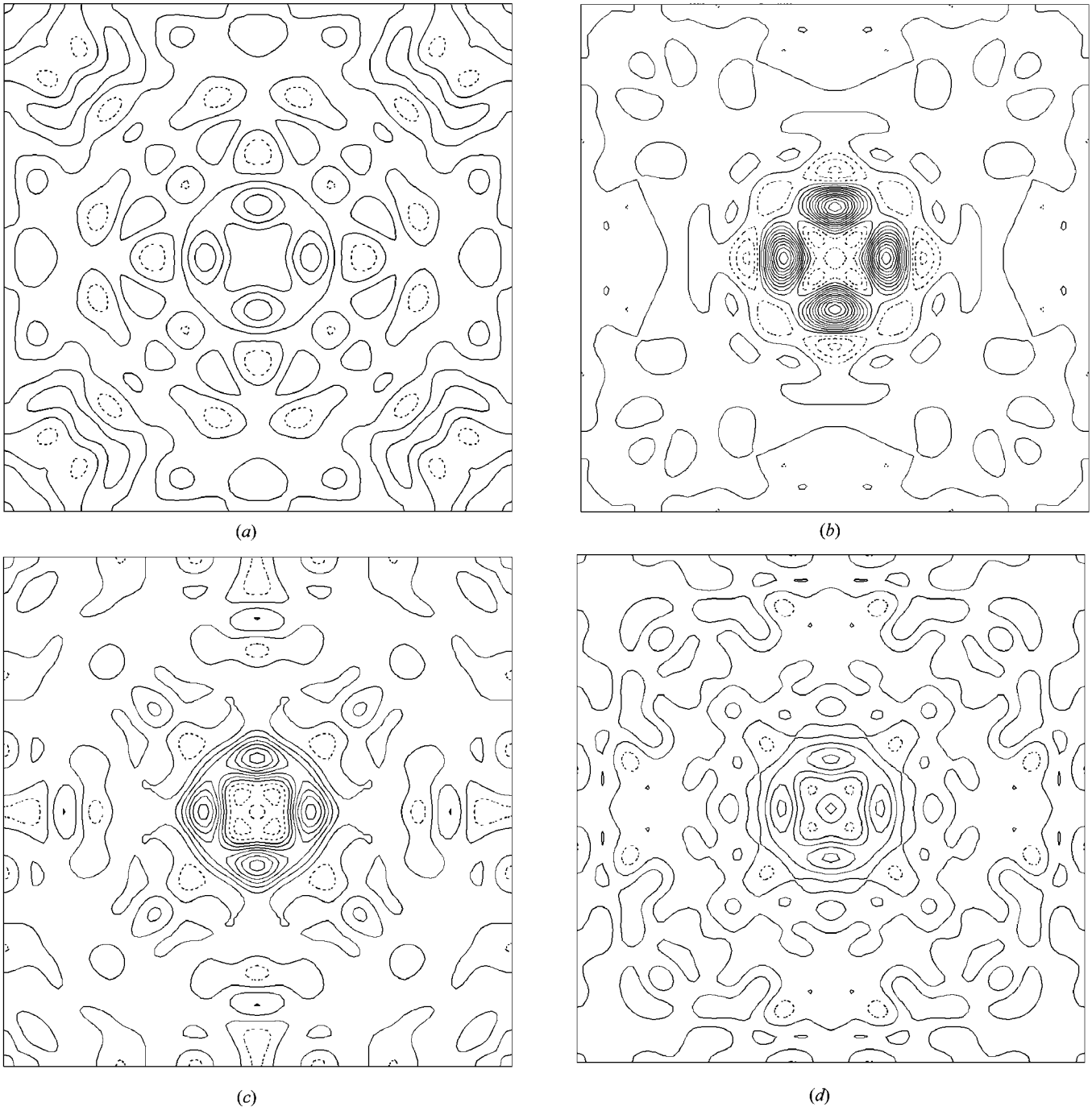

Figure 3
Deformation density after spherical-atom refinement at (*a*) 100, (*b*) 165, (*c*) 230 and (*d*) 298 K around Ce at $(\frac{1}{2}, \frac{1}{2}, \frac{1}{2})$ on the plane $z = \frac{1}{2}$ in the region $0 \leq x, y \leq 1$. Contours are at intervals of 0.2 e Å^{-3}. Zero and positive contours are drawn as full lines, while negative contours are drawn as broken lines.

where κ_i expresses an expansion ($\kappa_i < 1$) or contraction ($\kappa_i > 1$) of the ith AO. $\varphi_k(\kappa_i \mathbf{r})$ are the basis functions for the 4*f* orbitals. c_{ik}, κ_i and the electron population n_i can be refined. In the present case, there are no adjustable coefficients c_{ik} for the 4*f* orbitals because of the O_h crystal field around Ce.

When a strong-field model, where energy splitting of 4*f* states is dominated by a crystal field formed by negative ligands, is applied to 4*f* electrons in an O_h crystal field, seven *f* orbitals split into t_{1u}, t_{2u} and a_{2u} orbitals, expressed explicitly in terms of $|l, m\rangle = R_{nl}(r)Y_{lm}(\theta, \varphi)$ as

$$\begin{aligned} \psi_{x^3-3xy^2} &= -(\tfrac{1}{2}^{1/2})(|3,3\rangle - |3,-3\rangle), \\ \psi_{y^3-3yx^2} &= (i/2^{1/2})(|3,3\rangle + |3,-3\rangle), \\ \psi &= |3,0\rangle, \end{aligned} \tag{2}$$

for t_{1u} orbitals;

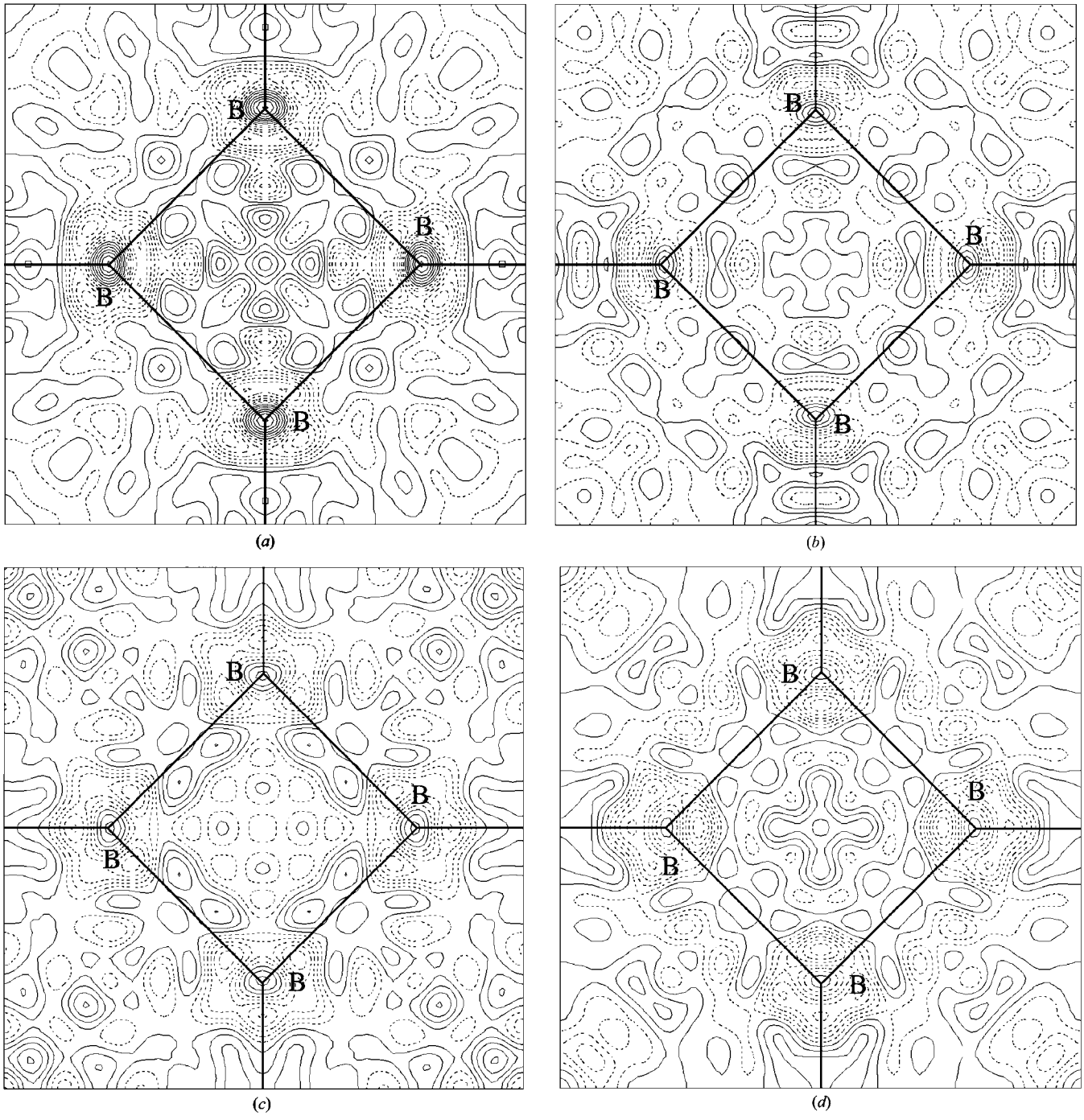

Figure 4
Deformation density after spherical-atom refinement at (*a*) 100, (*b*) 165, (*c*) 230 and (*d*) 298 K around the B_4 square on the plane $z = 0$ in the region $-0.5 \le x, y \le 0.5$. Contours are as in Fig. 3, except that the intervals are at 0.10 e Å^{-3}.

$$\begin{aligned}\psi_{5xz^2-xr^2} &= -(\tfrac{1}{2}^{1/2})(|3,1\rangle - |3,-1\rangle),\\ \psi_{5yz^2-yr^2} &= -(i/2^{1/2})(|3,1\rangle + |3,-1\rangle),\\ \psi_{z(x^2-y^2)} &= (\tfrac{1}{2}^{1/2})(|3,2\rangle + |3,-2\rangle),\end{aligned} \tag{3}$$

for t_{2u} orbitals; and

$$\psi_{xyz} = -(i/2^{1/2})(|3,2\rangle + |3,-2\rangle), \tag{4}$$

for the a_{2u} orbital. (r, θ, φ) are polar coordinates of electrons, Y_{lm} are spherical harmonics and $R_{43}(r)$ is the relativistic radial function for Ce. n, l and m are principal, azimuthal and magnetic quantum numbers, respectively. These seven orbitals can be treated as basis functions of an *f*-electron system and linear combinations of these orbitals can be treated in the program *QNTAO* [written by one of the authors (KT)]. In the

present case, they are also the eigenfunctions for a 4*f* electron in an O_h crystal field.

In a weak-field model, where the spin-orbit interaction is dominant over the crystal-field effect, ortho-normal basis functions for *f* orbitals, $|j, m\rangle$, are expressed in terms of orbital functions $|l, m_l\rangle$ and spin functions $|s, m_s\rangle$ as

$$|j, m\rangle = \sum_{m_l, m_s} |l, m_l\rangle|s, m_s\rangle\langle s, l;\ m_l, m_s|j, m\rangle, \quad -j \le m \le j, \tag{5}$$

where m is the sum of the magnetic and spin quantum numbers, m_l and m_s. $\langle s, l;\ m_l, m_s|j, m\rangle$ are tabulated by Condon & Shortley (1967). The explicit forms of $|j, m\rangle$ for *f* orbitals with $j = \frac{5}{2}$ are

$$\begin{aligned}
\left|\tfrac{5}{2}, \tfrac{5}{2}\right\rangle &= \tfrac{6}{7}^{1/2}\left|3, 3\right\rangle\left|\tfrac{1}{2}, -\tfrac{1}{2}\right\rangle - \tfrac{1}{7}^{1/2}\left|3, 2\right\rangle\left|\tfrac{1}{2}, \tfrac{1}{2}\right\rangle,\\
\left|\tfrac{5}{2}, \tfrac{3}{2}\right\rangle &= \tfrac{5}{7}^{1/2}\left|3, 2\right\rangle\left|\tfrac{1}{2}, -\tfrac{1}{2}\right\rangle - \tfrac{2}{7}^{1/2}\left|3, 1\right\rangle\left|\tfrac{1}{2}, \tfrac{1}{2}\right\rangle,\\
\left|\tfrac{5}{2}, \tfrac{1}{2}\right\rangle &= \tfrac{4}{7}^{1/2}\left|3, 1\right\rangle\left|\tfrac{1}{2}, -\tfrac{1}{2}\right\rangle - \tfrac{3}{7}^{1/2}\left|3, 0\right\rangle\left|\tfrac{1}{2}, \tfrac{1}{2}\right\rangle,\\
\left|\tfrac{5}{2}, -\tfrac{1}{2}\right\rangle &= \tfrac{3}{7}^{1/2}\left|3, 0\right\rangle\left|\tfrac{1}{2}, -\tfrac{1}{2}\right\rangle - \tfrac{4}{7}^{1/2}\left|3, -1\right\rangle\left|\tfrac{1}{2}, \tfrac{1}{2}\right\rangle,\\
\left|\tfrac{5}{2}, -\tfrac{3}{2}\right\rangle &= \tfrac{2}{7}^{1/2}\left|3, -1\right\rangle\left|\tfrac{1}{2}, -\tfrac{1}{2}\right\rangle - \tfrac{5}{7}^{1/2}\left|3, -2\right\rangle\left|\tfrac{1}{2}, \tfrac{1}{2}\right\rangle,\\
\left|\tfrac{5}{2}, -\tfrac{5}{2}\right\rangle &= \tfrac{1}{7}^{1/2}\left|3, -2\right\rangle\left|\tfrac{1}{2}, -\tfrac{1}{2}\right\rangle - \tfrac{6}{7}^{1/2}\left|3, -3\right\rangle\left|\tfrac{1}{2}, \tfrac{1}{2}\right\rangle.
\end{aligned} \tag{6}$$

In an O_h crystal field, *f* orbitals with $j = \frac{5}{2}$ split into twofold Γ_7 and fourfold Γ_8 orbitals. They are ortho-normal to each other and are expressed in terms of $|j, m\rangle$ as

$$\begin{aligned}
\left|\Gamma_7^{\alpha}\right\rangle &= \tfrac{1}{6}^{1/2}\left|\tfrac{5}{2}, \tfrac{5}{2}\right\rangle - \tfrac{5}{6}^{1/2}\left|\tfrac{5}{2}, -\tfrac{3}{2}\right\rangle,\\
\left|\Gamma_7^{\beta}\right\rangle &= \tfrac{1}{6}^{1/2}\left|\tfrac{5}{2}, -\tfrac{5}{2}\right\rangle - \tfrac{5}{6}^{1/2}\left|\tfrac{5}{2}, \tfrac{3}{2}\right\rangle,\\
\left|\Gamma_8^{\kappa}\right\rangle &= \tfrac{5}{6}^{1/2}\left|\tfrac{5}{2}, -\tfrac{5}{2}\right\rangle + \tfrac{1}{6}^{1/2}\left|\tfrac{5}{2}, \tfrac{3}{2}\right\rangle,\\
\left|\Gamma_8^{\upsilon}\right\rangle &= \tfrac{5}{6}^{1/2}\left|\tfrac{5}{2}, \tfrac{5}{2}\right\rangle + \tfrac{1}{6}^{1/2}\left|\tfrac{5}{2}, -\tfrac{3}{2}\right\rangle,\\
\left|\Gamma_8^{\lambda}\right\rangle &= \left|\tfrac{5}{2}, \tfrac{1}{2}\right\rangle,\\
\left|\Gamma_8^{\mu}\right\rangle &= \left|\tfrac{5}{2}, -\tfrac{1}{2}\right\rangle.
\end{aligned} \tag{7}$$

In the spin-orbit interaction model, basis functions have spin orbitals. However, they disappear in the X-ray scattering-factor formalism because of the orthogonal character of the two kinds of spin orbitals. The axes of quantization, x_q, y_q and z_q, were taken parallel to the lattice vectors, **a**, **b** and **c**, respectively, for Ce 4*f* and B 2*p* orbitals. Note that the main lobes of the Ce Γ_8 and Γ_7 orbitals distribute along the $\langle 100\rangle$ and $\langle 111\rangle$ directions, respectively, and B $2p_z$ extends along the B—B σ-bond between two B_6 octahedra and forms a main part of that bond. Since our measurement is not accurate enough to treat the overlap electrons between ligands and metal atoms (Tanaka, 1996), a molecular-orbital model or an orbital model consisting of an admixed orbital formed by the Ce 4*f* orbital with those of the conduction electrons of the ligands cannot be used within the framework of idempotency. Instead, simple 2*s*, $2p_x$, $2p_y$ and $2p_z$ orbitals were used for B, just to receive transferred 4*f* electrons and to keep the crystal neutral.

4. Refinement

4.1. Refinement with a spherical-atom model

Spherical-atom refinements for scale factors, atomic coordinates, anisotropic temperature factors and Type I anisotropic extinction parameters were carried out. Relativistic orbital functions of Ce^{3+} calculated with the program *HEX* by Liberman *et al.* (1971) and non-relativistic ones for $B^{-1/2}$ calculated by Mann (1968) were transferred to scattering factors with the program *SFSCF* [written by one of the authors (KT)]. Anomalous-dispersion terms were taken from the *International Tables for Crystallography* (1992, Vol. C). After the refinement, assuming Type I extinction (Becker & Coppens, 1974*a*,*b*, 1975) with a Thornley–Nelmes distribution function (Thornley & Nelmes, 1974), $R_1 = \sum ||F_o| - |F_c|| / \sum |F_o|$ and $R_2 = \left[\sum (|F_o| - |F_c|)^2 / \sum |F_o|^2\right]^{1/2}$ (both $\times 100$ when referred to as % values) were (0.0072, 0.0091), (0.0080, 0.0092), (0.0080, 0.0095) and (0.0091, 0.0101) at 100, 165, 230 and 298 K, respectively. F_o and F_c are the observed and calculated structure factors, respectively. Deformation densities around Ce and B_6 are shown in Figs. 3 and 4, respectively.

4.2. Refinement with a weak-field model

X-ray AO analysis was then carried out with the program *QNTAO*. In order to confirm that Γ_8 is the ground state, the population n and κ for Ce Γ_7 as well as Γ_8 orbitals were refined. Since Ce 5*p* orbitals are closest in energy to the 4*f* orbitals, n and κ of Ce $5p_{j=3/2}$ and $5p_{j=1/2}$ were also refined, keeping the unit cell electrically neutral using the following relation

$$\begin{aligned}
g_{\rm Ce}[n(\Gamma_8) + n(\Gamma_7) + n(5p_{j=5/2}) + n(5p_{j=3/2}) + 48]\\
+ g_{\rm B}[2n(p_x) + n(p_z) + 2] = g_{\rm Ce}Z_{\rm Ce} + g_{\rm B}Z_{\rm B},
\end{aligned} \tag{8}$$

where $g_{\rm Ce}$ and $g_{\rm B}$ are the multiplicities of Ce and B in the unit cell, respectively. $Z_{\rm Ce}$ and $Z_{\rm B}$ are the atomic numbers of Ce and B, respectively. When atomic sites are not fully occupied, multiplicities are refined while maintaining the relation (8), which is not the case in the present study. The remaining electrons of Ce were assumed to be core electrons. n and κ of B 2*s* and 2*p* orbitals were also refined. Those of B $2p_x$ and $2p_y$ were constrained to be the same since the refined B-atom location is at (0, 0, z) on the fourfold axis along the *c* axis.

Since the physical property of each parameter was quite clear and straightforward, refinement was conducted in a trial-and-error manner, adding a new parameter that was expected to be responsible for the largest residual peak. Finally, all the parameters were refined simultaneously, except those for harmonic and anharmonic temperature factors. Since the reduction in *R* factors, which were already less than 1% after the spherical-atom refinement (§4.1), was very small, the parameter was judged to be an effective one if the sum of the differences of the squares of F_o and F_c was reduced. Although parameter interaction in the least-squares analysis becomes more severe at higher temperature and the refinement

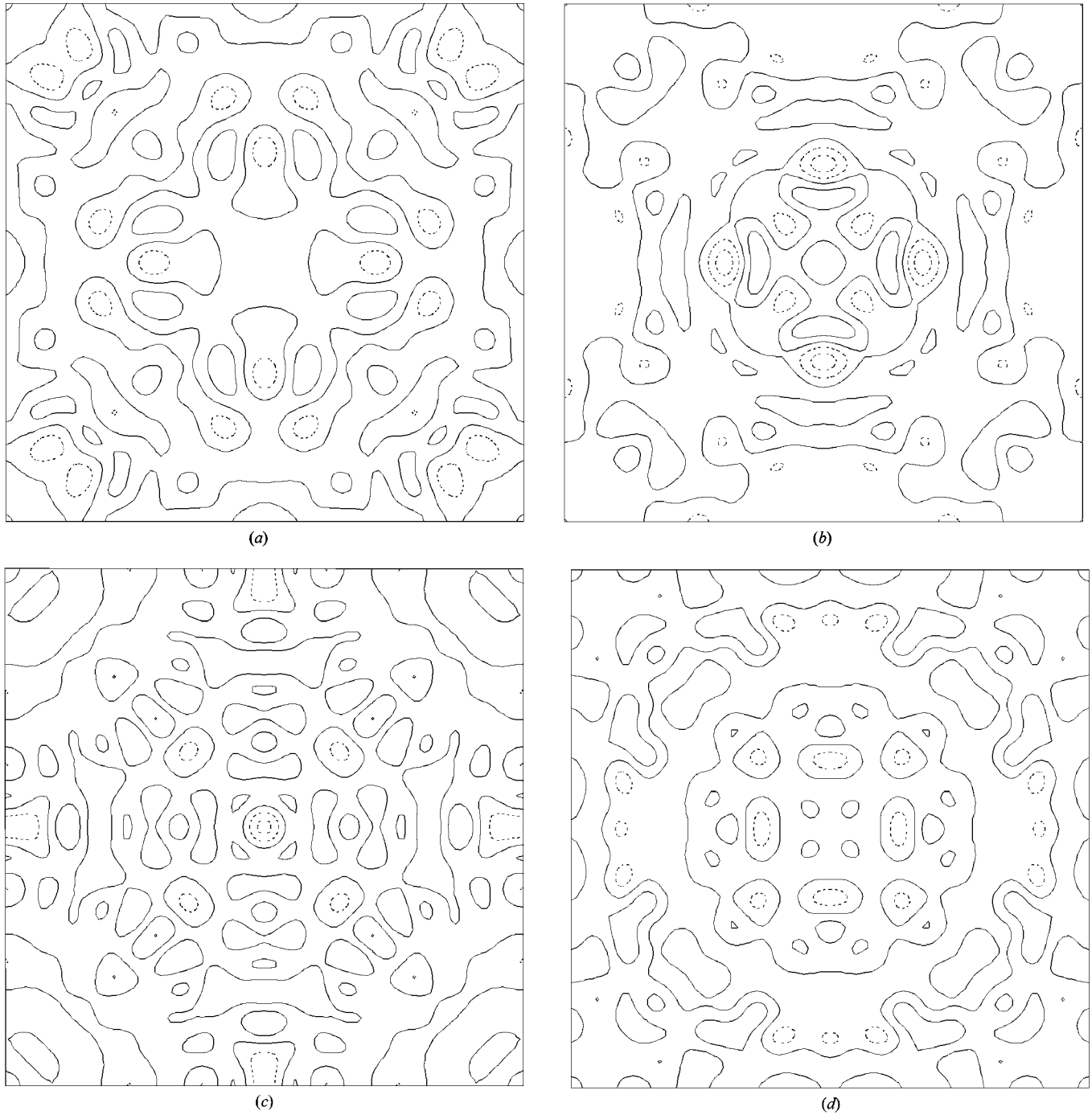

Figure 5
Deformation density after weak-field refinement at (*a*) 100, (*b*) 165, (*c*) 230 and (*d*) 298 K around Ce at $(\frac{1}{2}, \frac{1}{2}, \frac{1}{2})$ on the plane $z = \frac{1}{2}$ in the region $0 \leq x, y \leq 1$. Contours are as in Fig. 3.

procedures at the four temperatures are not exactly the same, the 'typical refinement' at 100 K is mainly described here.

At the first stage of the refinement, $\frac{1}{6}$ electron was allotted to each 4*f* orbital (two Γ_7 and four Γ_8 orbitals) and 1 electron was allotted to each 5*p* orbital, making the electron density around Ce spherical. Then the electron populations of the Ce 4*f* and 5*p* orbitals, and the B 2*s*, $2p_x$ and $2p_z$ orbitals, as well as the atomic and extinction parameters were refined. The population of the Γ_7 orbitals became negative at all the temperatures except at 298 K and was therefore fixed to zero. The refinement of the 298 K data was always unstable when the population of Γ_7 was varied. Therefore, the refinement at 298 K was continued with a fixed Γ_7 population of zero; it was only refined again at the last stage of the refinement. The populations of the Ce $5p_{j=3/2}$ and $5p_{j=1/2}$ orbitals were also fixed to 1 since they always tended to exceed their full occupation. The

Table 2
Extinction and final parameters.

(*a*) Parameters for *B* at (0, 0, *z*): fractional coordinate *z* ($\times10^{-4}$), temperature factors U^{ij} ($\times10^{-5}$ Å^2), population *n* ($\times10^{-2}$), κ ($\times10^{-2}$). Potential parameters: harmonic b_i ($\times10^{-21}$ J Å^{-2}), anharmonic cubic c_{ijk} ($\times10^{-19}$ Å^{-3}), anharmonic quartic q_{iijj} ($\times10^{-19}$ J Å^{-4}). Harmonic temperature factors are defined as $T_H = \exp(-2\pi^2 \sum_{i,j} h_i h_j a_i^* a_j^* U_{ij})$; anharmonic potentials V_a are defined in the text. For κ of Γ_7, see text.

	100 K	165 K	230 K	298 K
Ce				
U^{11}	227 (5)	347 (5)	450 (5)	577 (5)
$n(\Gamma_8)$	13 (1)	15 (2)	19 (2)	21 (2)
$n(\Gamma_7)$	0	0	0	4.2 (36)
$\kappa(\Gamma_8)$	179 (8)	158 (12)	157 (11)	160 (10)
$\kappa(5p_{j=3/2})$	95 (2)	98 (2)	100 (2)	100 (2)
b_1	608 (12)	657 (9)	706 (8)	713 (6)
q_{1111}	47 (19)	−14 (6)	0 (4)	6 (2)
q_{1122}	−131 (48)	39 (15)	−1 (11)	−13 (5)
B				
z	2984 (3)	2972 (3)	2963 (4)	2989 (4)
U^{11}	365 (12)	397 (12)	421 (14)	493 (13)
U^{33}	228 (11)	253 (14)	245 (18)	295 (23)
$n(2s)$	200	200	200	200
$n(2p_x)$	27 (6)	52 (4)	69 (4)	67 (4)
$n(2p_z)$	103 (8)	52 (8)	16 (8)	19 (8)
$\kappa(2s)$	99 (6)	98 (5)	103 (2)	104 (2)
$\kappa(2p_x)$	93 (31)	85 (16)	51 (19)	54 (17)
$\kappa(2p_z)$	92 (12)	108 (11)	130 (18)	130 (13)
b_1	378 (12)	575 (9)	755 (26)	835 (23)
b_3	607 (29)	900 (51)	1297 (97)	1393 (108)
c_{311}	6 (5)	−2 (6)	−9 (10)	4 (7)
c_{333}	−16 (9)	−17 (14)	−26 (26)	−18 (15)
q_{1111}	10 (33)	−32 (35)	19 (59)	35 (29)
q_{3333}	−244 (162)	−120 (154)	−296 (339)	39 (136)
q_{1122}	−359 (167)	68 (169)	−363 (275)	−160 (141)
q_{1133}	467 (293)	169 (278)	416 (567)	−64 (244)
R_1 (%)	0.64	0.67	0.70	0.83
R_2 (%)	0.80	0.76	0.81	0.90

(*b*) Anisotropic Type I extinction parameters with the Thornley–Nelmes distribution function.

	100 K	165 K	230 K	298 K
Y_{11}	99 (12)	86 (7)	39 (3)	62 (4)
Y_{22}	328 (42)	230 (18)	110 (10)	90 (7)
Y_{33}	71 (7)	44 (3)	27 (2)	24 (1)
Y_{12}	154 (20)	109 (10)	33 (4)	53 (4)
Y_{13}	−44 (7)	−26 (3)	−7 (1)	7 (1)
Y_{23}	−105 (14)	−61 (5)	−21 (2)	11 (1)

population of the B 2*s* orbital also exceeded 2, its full occupation, and was therefore fixed to 2. The R_1 and R_2 factors reduced to 0.0068 and 0.0086 after the population analysis. The population of Γ_8, however, was 0.68, which corresponds to 2.7 4*f* electrons on Ce. Then κ parameters were added as a variable and the $n(\Gamma_8)$ reduced to 0.22 at this stage, corresponding to 0.88 4*f* electrons on Ce. Refinement of $\kappa(5p_{j=1/2})$ always diverged and thus $5p_{j=1/2}$ was taken as one of the core orbitals. Since there was a severe parameter interaction between $n(\Gamma_8)$ and $\kappa(2p_x)$ of B at 298 K, they were refined separately.

Subsequently, anharmonic temperature factors were refined using the method of Tanaka & Marumo (1983), which is a general implementation of the method of Dawson *et al.* (1967)

Table 3
Parameters after strong-field refinements at 100, 165, 230 and 298 K.

For definitions of parameters, see Table 2.

	100 K	165 K	230 K	298 K
Ce				
U^{11}	228 (5)	345 (1)	452 (5)	576 (4)
$n(T_{1u})$	51 (13)	83 (8)	55 (13)	35 (23)
$n(T_{2u})$	57 (14)	0	43 (22)	63 (15)
$\kappa(T_{1u})$	146 (18)	172 (9)	132 (18)	141 (38)
$\kappa(T_{2u})$	227 (20)	–	215 (20)	162 (19)
q_{1111}	14 (19)	1 (6)	−3 (16)	0.9 (34)
q_{1122}	−53 (55)	−5 (17)	6 (45)	0.2 (101)
B				
z	3005 (2)	2973 (5)	3009 (2)	3000 (2)
U^{11}	356 (11)	388 (12)	412 (14)	472 (12)
U^{33}	232 (18)	252 (21)	242 (21)	309 (20)
$n(2s)$	200	200	200	200
$n(2p_x)$	28 (10)	39 (4)	34 (7)	32 (6)
$n(2p_z)$	57 (20)	47 (8)	50 (8)	54 (8)
$\kappa(2s)$	95 (14)	95 (4)	102 (4)	100 (4)
$\kappa(2p_x)$	95 (14)	96 (13)	68 (10)	89 (15)
$\kappa(2p_z)$	104 (7)	115 (8)	110 (11)	114 (10)
c_{311}	9 (6)	−21 (65)	11 (111)	15 (84)
c_{333}	−9 (9)	−174 (82)	−1 (253)	−71 (154)
q_{1111}	49 (32)	21 (62)	644 (516)	785 (299)
q_{3333}	−5 (26)	−47 (369)	−48 (420)	−74 (433)
q_{1122}	−318 (382)	38 (374)	−3852 (3078)	4789 (3488)
q_{1133}	29 (27)	−270 (375)	21 (774)	159 (446)
R_1 (%)	0.69	0.74	0.82	0.10
R_2 (%)	0.92	0.90	0.98	0.12

and Willis (1969) based on classical statistics. It assumes that intensity reduction by thermal vibrations of atoms is averaged with a weight, $\exp[-V(\mathbf{u})/kT]$, where *k* is the Boltzmann constant and $\mathbf{u}(u_1, u_2, u_3)$ is the displacement vector of an atom from its equilibrium position. The potentials $V(\mathbf{u})$ are expressed in terms of the displacement vector $\mathbf{u}(u_1, u_2, u_3)$ defined on the principal axes of the harmonic thermal ellipsoids, which were restricted to be parallel to the lattice vectors by the crystal symmetry. Since the point-group symmetries of Ce and B are $m\bar{3}m$ and $4mm$, respectively, the potentials are

$$V_{\rm Ce}(\mathbf{u}) = V_{0,\rm Ce} + \tfrac{1}{2}b_1 \sum_i \mathbf{u}_i^2 + q_{1111}(u_1^4 + u_2^4 + u_3^4) + q_{1122}(u_1^2u_2^2 + u_1^2u_3^2 + u_2^2u_3^2) \quad (9)$$

and

$$V_{\rm B}(\mathbf{u}) = V_{0,\rm B} + \tfrac{1}{2}[b_1(u_1^2 + u_2^2) + u_3^2] + c_{311}u_3(u_1^2 + u_2^2) + c_{333}u_3^3 + q_{1111}(u_1^4 + u_2^4) + q_{3333}u_3^4 + q_{1122}u_1^2u_2^2 + q_{1133}u_3^2(u_1^2 + u_2^2). \quad (10)$$

Coefficients in these equations were refined in the least-squares analysis with the other parameters. *R* factors were reduced to 0.0065 and 0.0080. The most severe problem in the refinement was parameter interaction between harmonic and anharmonic parameters. This means that partition of a potential into the second-, third- and fourth-order terms is somewhat ambiguous. The ambiguity arises from the larger errors of the higher-order reflections as a result of poor counting statistics since AHV is determined mainly by higher-order weak reflections, even though considerable time was

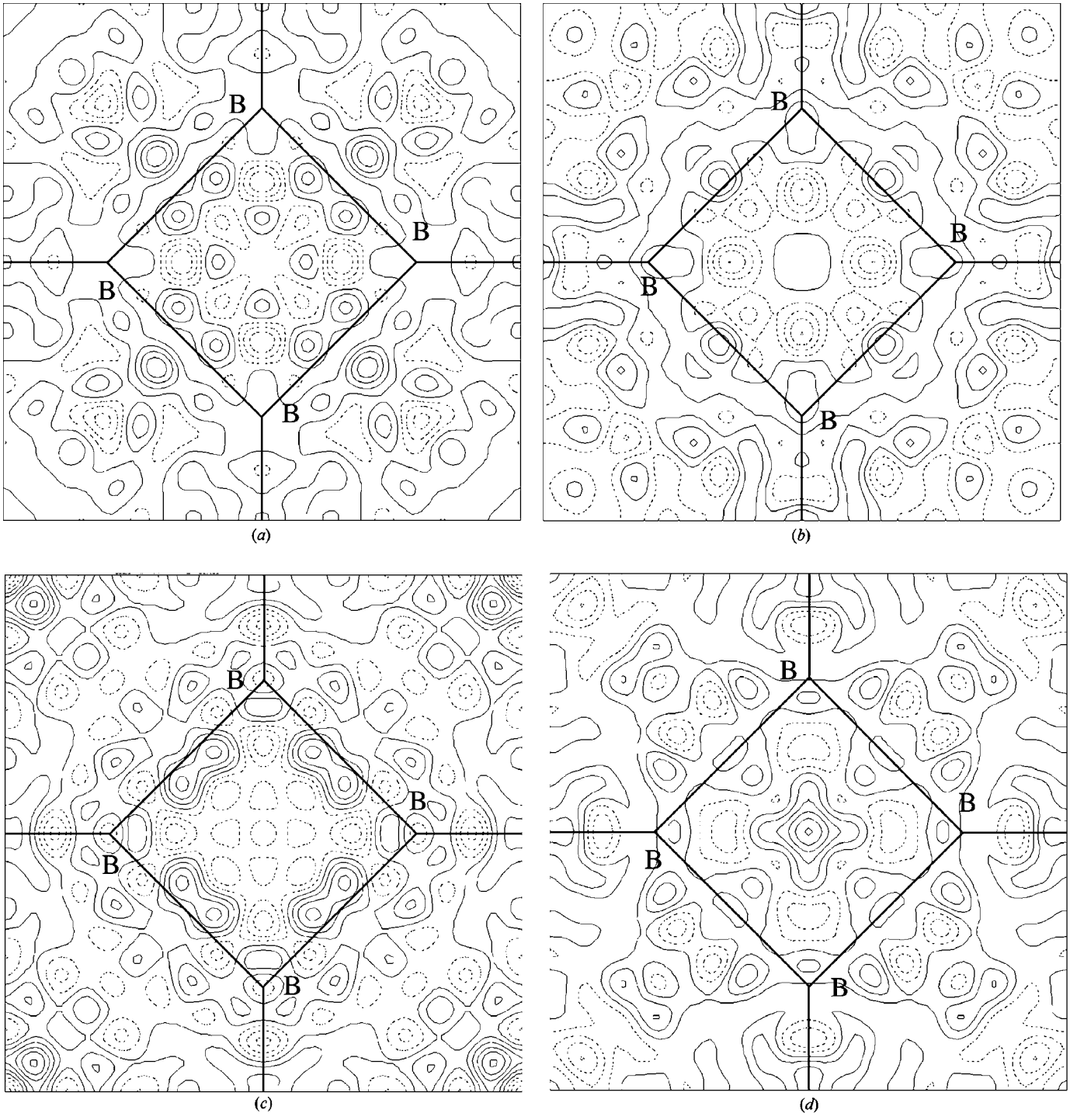

Figure 6
Deformation density after weak-field refinement at (*a*) 100, (*b*) 165, (*c*) 230 and (*d*) 298 K around the B_4 square on the plane $z = 0$ in the region $-0.5 \leq x, y \leq 0.5$. Contours are as in Fig. 4.

allotted for their measurement and there still exist very significant reflections even at $2\theta = 150^\circ$. Simultaneous refinements of the harmonic and anharmonic parameters converged to slightly smaller R factors, but resulted in unreasonable harmonic parameters of the B atom, which did not reduce with temperature. Therefore, harmonic and anharmonic parameters were refined separately, assuming that the harmonic potential is dominant over the anharmonic potential. The refinement of anharmonic parameters prior to κ parameters gave essentially the same result. Final R values and parameters are listed in Table 2. The residual densities around Ce and B are shown in Figs. 5 and 6, respectively. Along with the reduction in R factors compared with those of the spherical-atom model (Table 2), these data indicate that the refinements based on the weak-field model were successful. The ratio of the shift-to-error of $n(\Gamma_8)$ is 4.4×10^{-4}, which is the largest in

Table 4
Bond lengths.

	100 K	165 K	230 K	298 K
Ce—B (Å)	3.0416 (3)	3.0440 (4)	3.0459 (7)	3.0439 (4)
$(B-B)_{out}$ (Å)	1.6676 (17)	1.6782 (23)	1.6867 (35)	1.6644 (21)
$(B-B)_{in}$ (Å)	1.7459 (12)	1.7395 (16)	1.7341 (25)	1.7511 (7)

the final stage of the least-squares refinement at 100 K. Correlation coefficients with absolute values greater than 0.9 are those between two scale factors and $n(\Gamma_8)$, between q_{1111} and q_{1122} of Ce, between q_{1133} and q_{3333} of B, and those among the anisotropic extinction parameters.

4.3. Refinement with a strong-field model

The intensities measured at 100, 230 and 298 K were refined in the same manner as those at 165 K reported by TKŌ. At the first stage of the refinement, $\frac{1}{7}$ electron was allotted to each t_{1u}, t_{2u} and a_{2u} orbital; then they were allowed to shift with the other parameters. The population of the Ce a_{2u} orbital became negative and was fixed at zero. The population of the B 2*s* orbital tended to exceed 2 and was therefore fixed at 2, as in the weak-field model. However, the populations of the excited-state Ce t_{2u} orbital and the Ce t_{1u} orbital have significant values. Accordingly, these non-negative population parameters were refined with the conventional parameters; that is, the scale factors, the atomic coordinates, the temperature factors and Type I anisotropic extinction parameters, maintaining the electroneutrality of the unit cell. The κ parameters of all the populated orbitals of Ce and B were then refined with the other parameters. Parameters for AHV were subsequently refined with the usual parameters, except the harmonic temperature factors. They were refined separately, as described for the weak-field model. These processes were repeated several times. Final *R* values and parameters are listed in Table 3.

5. Results

5.1. Comparison between the weak- and strong-field models

Refinement with the weak-field model does not permit electrons to occupy the Γ_7 orbitals at low temperatures (100, 165 and 230 K); however, the strong-field model permits significant amounts of electrons to be in the first excited state T_{2u}, except at 165 K, as listed in Tables 2 and 3. The total electron population of the 4*f* orbitals in the weak-field model is always less than 1.0 and becomes smaller with decreasing temperature. In the strong-field model, the total number of 4*f* electrons ranges from 2.5 to 3.2 and does not decrease at lower temperatures. Results in Table 2 are correlated with one another systematically, in contrast to those in Table 3, indicating clearly that the week-field model fits better. Therefore, the following discussion is based on the results of the weak-field model only.

5.2. Basic structural change associated with the electron transfer

The lattice shrinks in CeB_6 when the temperature decreases, as indicated in Table 1, accompanying a continuous decrease in the population of the 4*f* electrons, as will be described in the next paragraph. The variation of bond lengths with temperature is presented in Table 4. The B—B bonds within a regular B_6 octahedron and between B_6 octahedra are denoted as $(B-B)_{in}$ and $(B-B)_{out}$, respectively. Bond lengths change smoothly with temperature, except those at 298 K. However, $(B-B)_{out}$ is shorter and $(B-B)_{in}$ is longer at 298 K than those at 100 K. This is correlated with the fact that a part of the electrons are thermally excited to Ce Γ_7 levels, as described in the next section. Since the crystal has one of the most closest-packed structures, the decrease in temperature from 230 to 100 K shrinks the lattice by only 0.00244 (9) Å (Table 1). However, changes in the crystal structure, the electron configuration and the vibration of the atoms are remarkable. $(B-B)_{out}$ becomes shorter by 0.019 (2) Å and $(B-B)_{in}$ gradually becomes longer by 0.012 (2) Å. Shorter $(B-B)_{out}$ bonds expand B_6 octahedra outward and make $(B-B)_{in}$ bonds longer, resulting in the tiny lattice shrinkage. It is also noteworthy that the shortest Ce—B distance changes only slightly.

5.3. Changes in electron configuration with decrease in temperature

The total number of 4*f* electrons, $4n(\Gamma_8) + 2n(\Gamma_7)$, decreases with lowering temperature: 0.98 (11), 0.77 (8), 0.61 (7), 0.52 (6). This decrease accompanies a very large contraction of Γ_8 and a small but significant expansion of the outermost $5p_{j=3/2}$ orbitals. Ce Γ_7 orbitals have no electrons, except at 298 K. $n(\Gamma_7)$ at 298 K is 0.042 (35) with $\kappa(\Gamma_7)$ = 0.8 (38). $n(\Gamma_7)/n(\Gamma_8)$ at 298 K corresponds to an energy gap of 470 (270) K, which agrees with that observed at 530 K (Sato *et al.*, 1984; Zirngiebl *et al.*, 1984; Loewenhaupt *et al.*, 1985) within experimental error, although the error is very large because of the large error in $n(\Gamma_7)$ and although $\kappa(\Gamma_7)$ is not significant.

B 2*s* is always fully occupied in the present study. The electron population $n(2p_z)$ in Table 2 is smaller than $n(2p_x)$ at 298 and 230 K. After becoming equal at 165 K, that is, the EDD around B is spherical, it becomes larger at 100 K. Evidently a part of the electrons in $2p_x$ and $2p_y$, as well as donated 4*f* electrons, moves to B $2p_z$. As listed in Table 2, the change in electron population of the 2*p* orbitals with a decrease in temperature is accompanied by a contraction of the $2p_x$ and expansion of the $2p_z$ orbitals compared with those at high temperatures.

5.4. Changes in EDD

The peaks around Ce in Figs. 3(*a*)–3(*d*) with heights of 0.6, 2.0, 1.2 and 0.6 e Å^{-3}, respectively, are not present in Figs. 5(*a*)–5(*d*) after the refinement based on a weak-field model. This indicates that the 4*f* electron configuration is described properly. However, the change of peaks around Ce at low

temperatures is very strange. In Fig. 3, the peaks around Ce are seen to be enhanced when the temperature was reduced from 230 to 165 K, in spite of the reduction of electron population, and then they decrease at 100 K. Moreover, the increase in peak heights by 0.8 e Å^{-3} at 165 K after losing 0.04 electrons from the Γ_8 state at 230 K looks too small compared with the decrease of peak heights by 1.4 e Å^{-3} at 100 K after losing 0.02 electrons from the state at 165 K.

In Fig. 4, each B—B bond in the octahedron has peaks just outside the line between the B atoms. Peaks around the $(B—B)_{out}$ bonds are higher than those of the $(B—B)_{in}$ bonds. There are positive and negative peaks in Fig. 4 on and around the B atom, respectively, at the four temperatures, which are not present in Fig. 6. The positive peaks just on the B atom in Fig. 4 have disappeared in Fig. 6, which suggests that the increase in the total number of 2*p* electrons due to the donated Ce 4*f* electrons has been taken into account properly in the X-ray AO analysis. The peaks on the $(B—B)_{out}$ bonds also reduce significantly in Fig. 6. Positive peaks along the ⟨100⟩ directions around the centre of the octahedron in Fig. 4 are also commonly seen at the four temperatures, although they are small at 230 K. They almost disappear, except at 298 K, where the peak at the origin becomes higher.

5.5. Changes in AHV

The anharmonic parameters of Ce in Table 2 become more prominent as temperature decreases. The variation of q_{1111} and q_{1122} of Ce with temperature is very complex. They are significant at 298 K and become insignificant at 230 K. Then they change their signs and become more significant. At 100 K they are larger than those at 165 K, but change their signs again. Negative c_{333} of B, which favours expansion of the B_6 octahedra along the $(B—B)_{out}$ bonds, is significant at all the temperatures except 230 K. This indicates that each B_6 octahedron has a tendency to expand with a decrease in temperature, which is also evident from the B—B bond lengths in Table 4. Negative and significant q_{3333} at 100 K also supports this case. Negative q_{1122} at all temperatures except at 165 K corresponds to favourable vibration of B along the directions perpendicular to the $(B—B)_{out}$ bonds. Large positive q_{1133} at 100 K is responsible for the negative peaks around B and along the $(B—B)_{in}$ bonds in Fig. 4(*a*), indicating that the $(B—B)_{in}$ bonds resist being shortened.

6. Discussion

The sum of electron populations of the four Γ_8 levels is less than 1 at the four temperatures and decreases with lowering temperature. Since the cancellation of 4*f* spins by the opposite spins of the conduction electrons by forming an admixed orbital constituted by the 4*f* orbital with the orbitals of the conduction electrons is the origin of the Kondo effect, the 4*f* electron transfer to the $(B—B)_{out}$ covalent bonds, which connect B_6 octahedra and are distributed throughout the crystal, is equivalent to the smaller coefficients of the 4*f* orbitals in the admixed orbital at the lower temperature. Therefore, the electron transfer is evidence that the Kondo effect in CeB_6 starts above room temperature and proceeds with a decrease in temperature. Although the B—B bonds are highly covalent and the present simple AO model cannot explain bonding electrons around bond centres (Fig. 6), and although a spherical part of the EDD seems to be too heavily partitioned to 2*s* orbitals, the electron configuration of B in Table 2 reflects the directional characteristics of the bonds. It evidently shows that more electrons on B $2p_x$ as well as Ce Γ_8 are transferred to B $2p_z$ at the lower temperature. Since the B $2p_z$ orbital has a main lobe along a $(B—B)_{out}$ bond, the increase in population and expansion of the orbital described in the foregoing section makes the $(B—B)_{out}$ bond stronger and shorter (Table 4). Localization of donated 4*f* electrons has been pointed out in CeNi, without specifying where they localize (Ōnuki, Kurosawa *et al.*, 1989).

In the foregoing section, two problems were pointed out after the X-ray AO analysis, namely, the strange variation of peak heights of 4*f* electron density with temperature and the enhancement of AHV at lower temperatures, which contradict our knowledge on EDD and AHV. Peaks of deformation densities usually become higher at lower temperature because of reduced atomic vibration, which seems true down to 165 K in spite of a decrease in $n(\Gamma_8)$. The peak reduction at 100 K is caused by a further decrease in $n(\Gamma_8)$. However, the change in the heights of 4*f* Γ_8 peaks is strange, as stated in the foregoing section. Usually, anharmonic thermal vibration becomes smaller at lower temperature because of reduced thermal vibration, except in unstable systems such as just before and after a phase transition (Sakata *et al.*, 1980; Tanaka & Nimura, 2002). Moreover, the temperature variation of q_{1111} and q_{1122} of Ce is also very strange. The strange behaviours of EDD and AHV at low temperatures are closely correlated. The negative q_{1111} of Ce at 165 K favours vibration along ⟨100⟩ directions or from Ce to the face-centres of the cubic lattice, resulting in the larger peaks in Fig. 3(*b*) than those expected from $n(\Gamma_8)$. On the other hand, positive q_{1111} at 100 K results in smaller peaks in Fig. 3(*a*).

The changes in AHV originate from the change in the effective atomic potential caused by the electron accumulation at B $2p_z$ and the significant expansion of the outermost $5p_{j=3/2}$ orbitals. B $2p_x$ (= $2p_y$) expands strongly at 298 and 230 K, as κ in Table 2 indicates, making the anharmonic vibration of positive Ce atoms along the ⟨110⟩ directions, which are from Ce to the centres of the $(B—B)_{out}$ bonds and bisect the main lobes of the Γ_8 orbitals, more favourable than along the ⟨100⟩ directions. Negative B atoms are also attracted along ⟨110⟩. This explains the negative q_{1122} of Ce and B in Table 2 at 298 K. Then B $2p_x$ begins to shrink at 165 K compared with that at higher temperatures, accompanying a decrease in $n(2p_x)$. This makes the vibration of Ce to vacant face-centres, that is, along ⟨100⟩, more favourable. Since Ce and $(B—B)_{out}$ become more positive and negative respectively at 100 K, and since occupied Γ_8 have main lobes along ⟨100⟩, the vibration along ⟨110⟩ becomes more favourable again. This is the reason for the large negative q_{1122} of $Ce^{3.48+}$ at 100 K. B $2p_x$ and $2p_y$ orbitals have lobes perpendicular to the cell edge with the

theoretical radial expectation value of 2.20 Å (Mann, 1968). They are closer to Ce than B $2p_z$ and their population and κ values determine the effect of the crystal field on the first approximation. The total EDD of the fully occupied $5p_{j=3/2}$ orbitals is spherical and the effect of the expansion is isotropic. Since CeB_6 has one of the most closest-packed structures, even a small expansion of the outermost orbitals is effective and reflects sharply a change in the crystal field. Since the Ce—B distance in Table 4 changes only slightly, the changes in $2p_x$ and $2p_y$ at lower temperatures reduce the effect of the crystal field. Therefore, the expansion at 165 and 100 K of Ce $5p_{j=3/2}$ corresponds to the weaker crystal field.

The relationships between $n(\Gamma_8)$ and κ of the Γ_8 and $5p_{j=3/2}$ orbitals are very interesting. A decrease in the population of Γ_8 usually indicates that the 4*f* orbitals become less stable with a decrease in temperature. However, $\kappa(\Gamma_8)$ values greater than 1.0 indicate that the Γ_8 orbitals, which are located inside the 5*p* orbitals, are strongly contracted, especially at 100 K, making Γ_8 more stable. A slight but significant decrease in κ of $5p_{j=3/2}$ in Table 2 also has an effect to reduce the energy of the Γ_8 state because of the lesser electrostatic repulsion between the Γ_8 and $5p_{j=3/2}$ electrons. These facts indicate that the system resists against losing 4*f* electrons from Ce by making Γ_8 more stable. This reminds us of the LeChátrier principle: the system resists against the change.

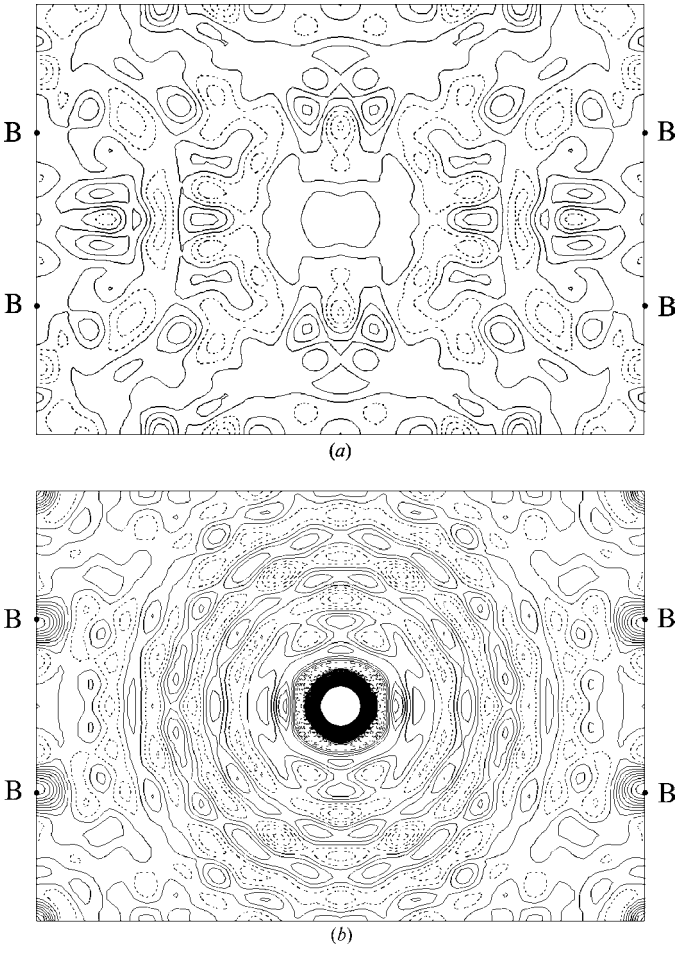

Figure 7
(*a*) Deformation density after weak-field refinement and (*b*) Fourier map at 100 K around Ce at $(\frac{1}{2}, \frac{1}{2}, \frac{1}{2})$ on the plane $x = y$. Ce and the origin are at the centre and upper left corner of the figure, respectively. Contours are at intervals of (*a*) 0.1 e Å^{-3} and (*b*) 5 e Å^{-3}.

Why are 4*f* electrons allowed to flow out of Ce in spite of the reduced energy of the Γ_8 state by the respective expansion and contraction of $5p_{j=3/2}$ and Γ_8? Since the present results tell us that the 4*f* electrons flow out of Ce, the energy loss caused by less electrons in more stable 4*f* Γ_8 states at lower temperature should be compensated. The enhanced AHV produces new vibration states along ⟨100⟩ and ⟨110⟩ at 165 and 100 K, respectively, increasing the ways to attain the energy of the system. The averaged effect is observed by X-ray diffraction as the enhancement of AHV. Therefore, the enhanced AHV at lower temperature means an increase in entropy. Since the electron donation from Ce to $(B—B)_{out}$ itself increases entropy, it cannot be stopped. As temperature approaches the Kondo temperature 2 K, AHV may not exist because of low kT at extremely low temperature. Energy gain by delocalization of 4*f* electrons throughout the crystal is expected to be the driving force of the change and $(B—B)_{out}$ is expected to be longer.

The discontinuous change in crystal structure at 298 K (Table 4) is very large, although n and κ of the Γ_8 and B 2*p* orbitals change only slightly. Since lobes of the Γ_7 orbitals point in ⟨111⟩ directions or to the centres of B_6 octahedra, and the $2p_x$ orbital still has a large electron population with large expansion (Table 2), B_6 octahedra expand outwards to reduce electrostatistic repulsion between B 2*p* and Ce Γ_7 electrons, making the $(B—B)_{out}$ bonds shorter without allotting significantly more electrons to B $2p_z$. The residual peak at the origin in Fig. 6(*d*) may be correlated to the Γ_7 electrons. Thus, the discontinuous changes in bond lengths and electron configuration at 298 K are correlated to thermal excitation of 4*f* electrons from Γ_8 to Γ_7, although the $n(\Gamma_7)$ is just significant.

As described in the foregoing discussion, the electron population of Ce Γ_8 is reduced with decreasing temperature and that of B $2p_z$ with a lobe toward $(B—B)_{out}$ increases. Since the t'_{1u} molecular orbital of B_6 is responsible for the $(B—B)_{out}$ bond (Longuet-Higgins & Roberts, 1954) and the t_{1u} Ce 4*f* orbital is an occupied orbital in a strong-crystal-field model, it is very interesting to search for the electron donation path on (110) where both t_{1u} orbitals coexist (see TK$\bar{O}$). Since Γ_8 orbitals are degenerate, linear combinations of them, $(|\Gamma_8^\nu\rangle \pm |\Gamma_8^\kappa\rangle)/2^{1/2}$ and $(\Gamma_8^\lambda\rangle \pm |\Gamma_8^\mu\rangle)/2^{1/2}$ are also eigenfunctions. It is easily seen that the main components of these are t_{1u} orbitals. The deformation density and Fourier maps at 100 K are shown in Figs. 7(*a*) and 7(*b*), respectively. The negative region between Ce and the centre of $(B—B)_{out}$ in Fig. 7(*a*) corresponds to the negative ripple of the Fourier map in Fig. 7(*b*) as a result of the series-termination effect. Residual densities on (001) in Fig. 5 also reveal electron density between Ce and $(B—B)_{out}$ bond centres at the corners of each figure. Although severe series-termination effects of the Fourier calculation have significant peaks in Fig. 7(*b*), both t_{1u} orbitals are connected with positive electron density and the Ce 4*f* electrons are expected to be donated through the 12

$(B-B)_{out}$ bonds around Ce. Generally, the series-termination effect on Fourier maps is expected to be very small on a deformation map. However, a comparison of Figs. 7(*a*) and 5(*a*) clearly shows that the residual peaks around Ce in Fig. 5(*a*) originate from the effect. CeB_6 is a hard crystal and even reflections with 2θ as high as 150° for Mo $K\alpha$ radiation are still strong enough to have such a strong series-termination effect.

AHV of atoms plays an important role in the present study and aspherical features of the EDD arising from the electron configuration itself and from the AHV were clearly discriminated. This discrimination should be possible, in principle, since the aspherical features of EDD and AHV mainly influence low- and high-order reflections, respectively. In practice, aspherical peaks arising from AHV have been found after the removal of those caused by aspherical *d* electrons in $KCuF_3$ (Tanaka & Marumo, 1982), $CuAlO_2$ (Ishiguro *et al.*, 1982) and $[Cu(diazacyclooctane)_2](NO_3)_2$ (Tanaka, 1993). In our method, based on Boltzmann statistics, AHV and EDD are expressed in terms of functions of quite different type, which makes the distinction between these effects possible. Moreover, the correction terms for AHV in the structure-factor formalism are defined quite clearly based on the vibration of atoms and are expressed in terms of harmonic potential parameters as well as anharmonic ones [equation (6)] (Tanaka & Marumo, 1983). These features of our method restrict the inclusion of aspherical EDD into temperature factors, although interactions between harmonic and anharmonic parameters are usually severe. Therefore, our method has less room for the inclusion of aspherical features of EDD resulting from the electron configuration than the other statistical correction methods for AHV.

7. Conclusion

4*f* Electron density was observed after avoiding multiple diffraction and the weak-field model was successfully applied to the analysis of EDD in CeB_6. At different temperatures, the relationships among crystal structure, EDD, electron population *n*, the expansion/contraction parameters κ and parameters for AHV were quite consistent with one another, although they looked contradictory at first sight. Therefore, we first conclude that the 4*f* electron densities were measured and analysed quit well, thus opening the door to measurements and analyses of the EDD of heavy-atom crystals by X-ray diffraction.

Since the origin of AHV is explained rationally from the electron transfer in CeB_6 and since the deformation densities can be explained in terms of AHV quite well, the present results confirm again that aspherical features in the deformation density resulting from the electron configuration itself and those resulting from AHV can be separated. The process of the 4*f*-electron transfer from Ce to $(B-B)_{out}$ was explained in terms of the enhanced AHV at low temperature and was concluded to be an entropy-driven transfer within the temperature range of the present measurements. The present study, to our knowledge, is the first research on the temperature dependence of EDD that reveals the role of entropy during the change of a system.

The energy gap between the Γ_7 and Γ_8 orbitals was obtained from X-ray diffraction experiments, though the error is large because of a large error in $n(\Gamma_7)$. This will be improved when the accuracy of the structure-factor measurements is improved. Significant $n(\Gamma_7)$ showed that a thermal excitation from the Γ_7 to the Γ_8 level occurred. This is also supported by discontinuous changes in the bond lengths at 298 K, which are explained through a directional characteristic of the Γ_7 orbitals. However, further experiments are necessary to confirm these results.

The present multi-temperature measurements of EDD reveal very clearly its advantages in investigations of the changes of a system with temperature, as well as in assessing results that were supposed to be almost impossible. Multi-dimensional X-ray diffraction analysis in which temperature, time and energy are added as experimental variables to the three dimensions of space will be a very fascinating field in science.

We thank Professors T. Okuda, I. Sakamoto and N. Shida of Nagoya Institute of Technology for helpful comments and discussions. This work was supported by funding from the JST under the project of CREST.

References

Becker, P. J. & Coppens, P. (1974*a*). *Acta Cryst.* A**30**, 129–147.
Becker, P. J. & Coppens, P. (1974*b*). *Acta Cryst.* A**30**, 148–153.
Becker, P. J. & Coppens, P. (1975). *Acta Cryst.* A**31**, 417–425.
Boulay, D. du, Maslen, E. N. & Streltsov, V. A. (1995). *Acta Cryst.* B**51**, 921–929.
Chatterjee, A., Maslen, E. N. & Watson, K. J. (1988). *Acta Cryst.* B**44**, 386–395.
Condon, E. U. & Shortley, G. H. (1967). *The Theory of Atomic Spectra*. Cambridge University Press.
Dawson, B., Hurley, A. C. & Maslen, V. W. (1967). *Proc. R. Soc. London Ser. A*, **298**, 289–306.
Ishiguro, T., Ishizawa, B., Mizutani, N., Kato, M., Tanaka. K. & Marumo, F. (1982). *Acta Cryst.* B**39**, 564–569.
Liberman, A., Cromer, D. T. & Waber, J. T. (1971). *Comput. Phys. Commun.* **2**, 107–113.
Loewenhaupt, M., Carpenter, J. M. & Loong, C.-K. (1985). *J. Magn. Magn. Mater.* **52**, 245–249.
Longuet-Higgins, H. C. & Roberts, M. de V. (1954). *Proc. R. Soc. London Ser. A*, **224**, 336–347.
Makarova, I. P., Bram, A., Burzlaff, H., Blomberg, M., Merisalo, M. & Simonov, V. I. (1995). *J. Alloys Compd*, **225**, 599–603.
Mann, J. B. (1968). Report LA3691. Los Alamos National Laboratory, New Mexico, USA.
Maslen, E. N., Streltsov, V. A. & Ishizawa, N. (1996*a*). *Acta Cryst.* B**52**, 406–413.
Maslen, E. N., Streltsov, V. A. & Ishizawa, N. (1996*b*). *Acta Cryst.* B**52**, 414–422.
Ōnuki, Y., Furukawa, Y. & Komatsubara, T. (1984) *J. Phys. Soc. Jpn*, **53**, 2734–2740.
Ōnuki, Y., Komatsubara, T., Reiders, P. H. P. & Springford, M. (1989). *J. Phys. Soc. Jpn*, **58**, 3698–3704.
Ōnuki, Y., Kurosawa, Y., Maezawa, K., Umehara, I., Isikawa, K. & Sato, K. (1989). *J. Phys. Soc. Jpn*, **58**, 3705–3710.
Sakata, M., Harada, J., Cooper, M. J. & Rouse, K. D. (1980). *Acta Cryst.* A**36**, 7–15.

Sato, S. (1985). *J. Magn. Magn. Mater.* **52**, 310–312.
Sato, N., Kunii, S., Oguro, I., Komatsuzawa, T. & Kasuya, T. (1984). *J. Phys. Soc. Jpn*, **53**, 3967–3979.
Shoemaker, D. (1968). *Acta Cryst.* A**24**, 136–142.
Streltsov, V. A. & Ishizawa, N. (1999). *Acta Cryst.* B**55**, 1–7.
Streltsov, V. A., Konovalova, E. S., Paderno, Yu. B. (1999). *Physica B*, **259–261**, 1155–1156.
Tanaka, K. (1988). *Acta Cryst.* A**35**, 1002–1008.
Tanaka, K. (1993). *Acta Cryst.* B**49**, 1001–1010.
Tanaka, K. (1996). *Mol. Cryst. Liq. Cryst.* **278**, 111–116.
Tanaka, K., Kato, Y. & Ōnuki, Y. (1997). *Acta Cryst.* B**53**, 143–152.
Tanaka, K., Kumazawa, S., Tsubokawa, M., Maruno, S. & Shirotani, I. (1994). *Acta Cryst.* A**50**, 246–252.
Tanaka, K. & Marumo F. (1982). *Acta Cryst.* A**38**, 1422–1427.
Tanaka, K. & Marumo F. (1983). *Acta Cryst.* A**39**, 631–641.
Tanaka, K. & Nimura, T. (2002). To be published.
Thornley, F. R. & Nelmes, R. J. (1974). *Acta Cryst.* A**30**, 748–757.
Willis, B. T. M. (1969). *Acta Cryst.* A**25**, 277–300.
Zirngiebl, E., Hillerbrands, B., Blumenröder, S., Guntherodt, G., Loewenhaupt, M., Carpenter, J. M., Winzer, K. & Fisk, Z. (1984). *Phys. Rev. B*, **30**, 4052–4054.